Nanoscale

PAPER

View Article Online
View Journal | View Issue

Cite this: *Nanoscale*, 2016, **8**, 12560

# Magnetically targeted delivery of DOX loaded $Cu_9S_5$@$mSiO_2$@$Fe_3O_4$-PEG nanocomposites for combined MR imaging and chemo/photothermal synergistic therapy

Bei Liu,[a,d] Xinyang Zhang,[a] Chunxia Li,*[a] Fei He,[a,d] Yinyin Chen,[a,d] Shanshan Huang,[a] Dayong Jin,[b] Piaoping Yang,[c] Ziyong Cheng[a] and Jun Lin*[a]

Received 14th September 2015,
Accepted 27th October 2015

DOI: 10.1039/c5nr06322a

www.rsc.org/nanoscale

The combination of multi-theranostic modes in a controlled fashion has received tremendous attention for the construction of cooperative therapeutic systems in nanomedicine. Herein, we have synthesized a smart magnetically targeted nanocarrier system, $Cu_9S_5$@$mSiO_2$@$Fe_3O_4$-PEG (labelled as CMF), which integrates NIR triggered photothermal therapy, pH/NIR-responsive chemotherapy and MR imaging into one nanoplatform to enhance the therapeutic efficacy. This new multifunctional paradigm has a uniform and monodisperse sesame ball-like structure by decorating tiny $Fe_3O_4$ nanoparticles on the surface of $Cu_9S_5$@$mSiO_2$ before a further PEG modification to improve its hydrophilicity and biocompatibility. With doxorubicin (DOX) payload, the as-obtained CMF-DOX composites can simultaneously provide an intense heating effect and enhanced DOX release upon 980 nm NIR light exposure, achieving a combined chemo/photothermal therapy. Under the influence of an external magnetic field, the magnetically targeted synergistic therapeutic effect of CMF-DOX can lead to highly superior inhibition of animal H22 tumor *in vivo* when compared to any of the single approaches alone. The results revealed that this $Cu_9S_5$ based magnetically targeted chemo/photothermal synergistic nanocarrier system has great promise in future MR imaging assisted tumor targeted therapy of cancer.

## 1. Introduction

Recently, there has been a growing interest in combating cancer with external stimulus-sensitive drug delivering nanocarriers because they can differentially increase the drug accumulation at targeted cancer cells, drastically decrease the systemic toxicity, and potentially avoid under- or overdosing.[1–3] Among them, light-responsive vehicles, especially plasmonic nanomaterials that can convert near-infrared (NIR) light into heat energy for localized photothermal therapy (PTT), have gained a rapid development owning to their minimally invasive therapeutic properties and potentially effective cancer therapy.[4–6] Many types of nanomaterials with strong NIR absorbance have been developed for the photothermal treatment of cancer such as noble metal nanostructures,[7–9] carbon-based materials,[10,11] organic compounds[12,13] and semiconductor compounds.[14,15] Among them, one of the recently developed and promising candidates is $Cu_9S_5$ nanoparticles, owning to their advanced properties such as low cost, high stability, low cytotoxicity and their intrinsic NIR region absorption derived from d–d energy band transitions.[16–19] However, photothermal therapy sometimes fails to eradicate tumor cells at once owning to the inhomogeneous heat distribution within tumor tissues, thus resulting in inevitable tumor recurrence and metastasis. Therefore, the idea of combining $Cu_9S_5$ based photothermal ablation therapy with other therapeutic methods has become attractive to treat cancers and overcome drug resistance in current cancer-therapy research fields.

Among various combination therapies, the efficient combination of photothermal ablation with conventional chemotherapy can not only significantly increase the synergistic antitumor efficacy when compared to the individual treatments, but also promote drug release and thus, achieve an enhanced chemotherapy effect.[20,21] Therefore, exploration on NIR-responsive photothermal agents potentially engineered as drug vehicles to achieve an enhanced anticancer effect is highly desirable and

---

[a] State Key Laboratory of Rare Earth Resource Utilization, Changchun Institute of Applied Chemistry, Chinese Academy of Sciences, Changchun, 130022, P. R. China. E-mail: jlin@ciac.ac.cn, cxli@ciac.ac.cn; Fax: +86-431-85698041; Tel: +86-431-85262031

[b] Institute for Biomedical Materials and Devices, Faculty of Science, University of Technology Sydney, NSW, 2007, Australia

[c] Key Laboratory of Superlight Materials and Surface Technology, Ministry of Education, College of Material Sciences and Chemical Engineering, Harbin Engineering University, Harbin 150001, PR China

[d] University of Chinese Academy of Sciences, Beijing, 100049, China

important. In general, there are two major strategies to develop these types of nanometer-sized nanocarrier systems: one is the direct loading of anticancer drugs into photothermal conversion agents, such as gold nanocages[22] and hollow copper sulphide,[23] using chemical interactions or electrostatic adsorption; another typical approach is the combination of photothermal conversion agents with drug-loaded mesoporous material/organic compounds, *e.g.* mesoporous silica-coated $Cu_{2-x}Se$ nanoparticles,[24] gold nanoshells on silica nanorattles,[25,26] and gold nanorods-capped magnetic core/mesoporous silica shell nanoellipsoids.[27] However, the major hurdle of these photothermal nanocarriers lies in their low accumulation concentration at the targeted location, thus resulting in high toxic side effects to the healthy tissues as well as unspecific uptake in normal cells. To solve these problems, a further modification should be carried out for targeted delivery applications. Among the various modification methods, the use of magnetic nanoparticles as a targeted drug delivering agent under the influence of an external magnetic field has received a lot of attention, based on their low cost, ease of preparation, low toxicity and ability to tailor their properties for specific biological applications.[28–30] Furthermore, the magnetic nanoparticles can also act as a $T_2$ weighted magnetic resonance (MR) contrast agent, which can help to integrate MR imaging with non-invasive character and high spatial resolution into this therapeutic platform.[31,32] From the above-mentioned discussion and analysis, we can conclude that combining the merits of magnetically targeted chemo/photothermal therapy with MR imaging ensures a promising drug delivery vehicle for advanced therapeutic purposes.

In the present study, we have successfully synthesized a multifunctional magnetically targeted chemo/photothermal therapy system, $Cu_9S_5@mSiO_2@Fe_3O_4$-PEG (labelled as CMF), employing $Cu_9S_5$ as the photo-absorbing agent, mesoporous $SiO_2$ shell as the drug carrier vehicle, $Fe_3O_4$ nanoparticles as the magnetically targeted probe and $T_2$ MR contrast agent and PEG modification to improve its biocompatibility. The as-obtained uniform, monodisperse and sesame ball-like CMF nanoparticles can simultaneously provide both a magnetically targeted chemo/photothermal therapy upon NIR exposure and effective MR imaging with $T_2$ contrast abilities, providing a new possibility for the synergistic diagnosis and therapy of cancer. The pH/NIR depended drug delivery properties, MR imaging, *in vitro*/*in vivo* biocompatibility tests as well as the magnetically targeted chemotherapy/hyperthermia of CMF were investigated in detail. Furthermore, Haematoxylin and Eosin (H&E) staining of main organs, including the heart, liver, spleen, lung, and kidney, was also carried out to further investigate the *in vivo* biocompatibility.

## 2. Results and discussion

### 2.1 The controlled fabrication and characterization of $Cu_9S_5@mSiO_2@Fe_3O_4$-PEG (CMF)

Tumor site-directed multifunctional theranostic nanoplatforms have been in high demand in recent years for effective cancer therapy.[33] Herein, a low toxic multifunctional nanoplatform, $Cu_9S_5@mSiO_2@Fe_3O_4$-PEG (labelled as CMF), integrating both MR imaging and magnetically targeted chemo/photothermal antitumor therapy was successfully fabricated and developed. In this anticancer therapy system, as illustrated in Scheme 1, every part plays its own role: the core of $Cu_9S_5$ provides a high NIR photothermal conversion efficiency, the mesoporous $SiO_2$ shell guarantees excellent anticancer drug loading, the decorated $Fe_3O_4$ nanoparticles facilitate CMF nanoparticles for magnetically targeted delivery and $T_2$ enhanced MR imaging, whereas PEGylation ensures biocompatibility. The overall fabrication procedure of CMF is illustrated in Fig. 1a. First, hydrophobic $Cu_9S_5$ nanocrystals with a uniform size of 18 nm (Fig. 1b) were successfully synthesized and then transferred into an aqueous phase utilizing cetyltrimethyl ammonium bromide (CTAB) as a secondary surfactant. Second, the as-obtained $Cu_9S_5$–CTAB were coated with a

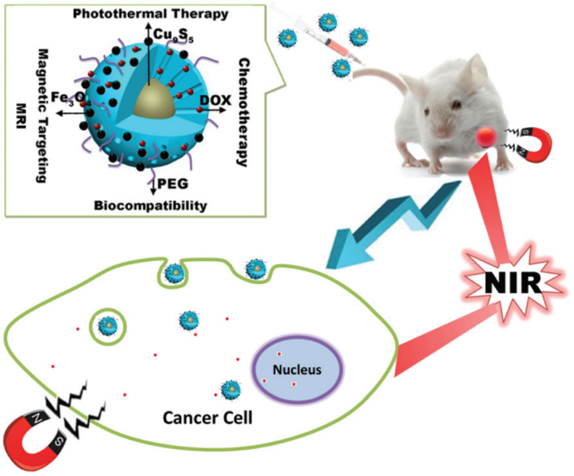

Scheme 1 A schematic of the $Cu_9S_5@mSiO_2@Fe_3O_4$-PEG (labelled as CMF) nanocomposites used for combined MR imaging and magnetically targeted chemo/photothermal synergistic therapy.

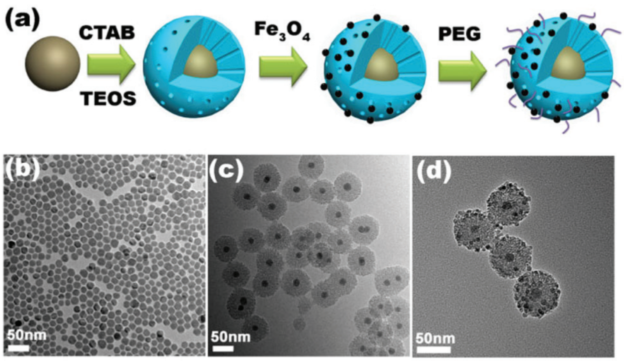

Fig. 1 (a) A schematic of the synthesis of the core–shell structured CMF nanocomposites. (b–d) TEM images of $Cu_9S_5$ (b), $Cu_9S_5@mSiO_2$ (c) and $Cu_9S_5@mSiO_2@Fe_3O_4$-PEG (d).

uniform silica shell using a phase-transfer-assisted surfactant-template coating process, forming $Cu_9S_5@mSiO_2$ core–shell composite nanoparticles (Fig. 1c). The CTAB template was then removed thoroughly *via* an ion exchange method. Third, the as-synthesized $Cu_9S_5@mSiO_2$ nanospheres were further modified with amine groups, which can serve as both the $Fe_3O_4$ and PEG anchor points in the following reaction steps. Then, the ultra small $Fe_3O_4$ nanoparticles can be successfully decorated *via* a nucleophilic substitution reaction onto the surface of the $Cu_9S_5@mSiO_2$ nanospheres, resulting in the formation of $Cu_9S_5@mSiO_2@Fe_3O_4$. As shown in Fig. 1d and 2a, the as-synthesized $Cu_9S_5@mSiO_2@Fe_3O_4$ nanoparticles have the same morphology as $Cu_9S_5@mSiO_2$, except for the successful decoration of ultra small $Fe_3O_4$ nanocrystals (about 5 nm) on their surface. It is worth noting that the tiny $Fe_3O_4$ nanocrystals can play two important roles in the following bio-applications: (i) As a $T_2$ positive agent for the MR imaging and (ii) as a magnetic targeting factor in the combined chemo/photothermal therapy. Finally, PEG was chosen to modify the as-obtained $Cu_9S_5@mSiO_2@Fe_3O_4$ nanocomposites to improve their colloidal stability and eliminate hemolysis induced by the silica nanoparticles *via* the formation of a biocompatible layer.[34] Due to the presence of the PEG ligands on their surface, the as-prepared CMF nanoparticles are hydrophilic and can be readily dispersed in water. The HRTEM image is given in Fig. 2b, which shows that the interplanar spacing of the lattice fringes is 0.25 nm, indexed to the (311) plane of $Fe_3O_4$. Moreover, the corresponding HAADF-STEM-EDS mapping images shown in Fig. 2c–g can help to further verify the successful construction of the core/shell/satellite CMF nanoparticles. The XRD patterns of $Cu_9S_5$, $Fe_3O_4$ and $Cu_9S_5@mSiO_2$ are shown in Fig. 2h, from which we can observe that the diffraction peaks of $Cu_9S_5$ and $Fe_3O_4$ can be indexed as the pure cubic phase structure of $Cu_9S_5$ (JCPDS 47-1748) and $Fe_3O_4$ (JCPDS 19-0629), respectively, whereas the $Cu_9S_5@mSiO_2$ was mainly ascribed to the $Cu_9S_5$ structure besides an amorphous silica structure peak at $2\theta = 22°$. The XRD patterns of $Cu_9S_5@mSiO_2@Fe_3O_4$ are not given here because their diffraction peaks do not show any difference when compared with those found for $Cu_9S_5@mSiO_2$, mainly because of the low concentration and small size of $Fe_3O_4$ in the CMF nanocomposites. The $N_2$ adsorption/desorption isotherm shown in Fig. 2i shows a type-IV isotherm, which is typical for mesoporous materials. The corresponding pore size distribution of the CMF nanospheres is very uniform with an average size of 2.4 nm (see the inset of Fig. 2i). These results indicate that the mesoporous silica shell of CMF is suitable for loading a sufficient amount of a drug in chemotherapy applications.[35] Moreover, because of the successful decoration of $Fe_3O_4$ on the surface of $Cu_9S_5@mSiO_2$, the magnetic targeting properties of the CMF were evaluated by adding a magnet on the side of cuvette containing the CMF aqueous solution. Fig. 2j shows that the CMF nanoparticles can be trapped directly to the neighboring magnet, suggesting that the as-obtained CMF nanoparticles can be used as magnetic targeting factors in the following anticancer therapies.

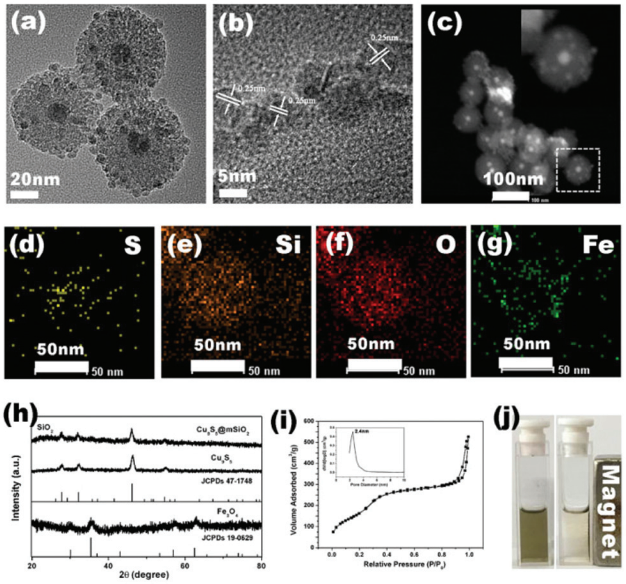

**Fig. 2** (a) TEM image of $Cu_9S_5@mSiO_2@Fe_3O_4$-PEG. (b) HRTEM image of the $Fe_3O_4$ decorated on the surface of $Cu_9S_5@mSiO_2$. (c) High angle annular dark field scanning transmission electron microscopy (HAADF-STEM) images of the $Cu_9S_5@mSiO_2@Fe_3O_4$ nanoparticles and (d–g) HAADF-STEM-EDS mapping images of the $Cu_9S_5@mSiO_2@Fe_3O_4$ nanoparticles. (h) XRD patterns of the as-prepared $Cu_9S_5$, $Cu_9S_5@mSiO_2$, $Fe_3O_4$ and the corresponding standard data of $Cu_9S_5$ (JCPDS no. 47-1748) and $Fe_3O_4$ (JCPDS 19-0629). (i) $N_2$ adsorption–desorption isotherms and mesopore size distribution (inset) of CMF. (j) Images of the CMF samples (0.2 mg $mL^{-1}$) in an aqueous solution under ambient light (left) and with a neighbouring magnet (right).

## 2.2 The photothermal effect and drug loading capacity of CMF

Because of the presence of $Cu_9S_5$ nanoparticles in their core, CMF nanoparticles are endowed with a distinct photothermal conversion performance.[36] The absorption spectrum of the aqueous $Cu_9S_5@mSiO_2$ nanocomposite solution (0.5 mg $mL^{-1}$) was examined by UV-vis-NIR spectroscopy, as shown in Fig. 3a. The spectrum exhibits a minimum absorption at around 630 nm. With an increasing wavelength from 630 to 1100 nm, the absorption intensity increases, showing a relatively strong absorption at a wavelength of 980 nm. Therefore, the as-synthesized CMF nanocomposites have great potential for photothermal conversion bio-applications under irradiation at 980 nm. To further evaluate their photothermal conversion, aqueous dispersions of CMF at different concentrations were irradiated at 980 nm with a power density of 0.76 W $cm^{-2}$ for 5 min and the temperature recorded, as shown in Fig. 3b. As shown in these temperature variation curves, significant heating of the solution was observed, especially at high CMF concentrations, whereas only a slight temperature increase was observed in pure water. With a 1 mg $mL^{-1}$ CMF aqueous solution, the temperature increased by 23.2 °C in 5 min, whereas pure water increased by only 6.1 °C (Fig. 3c), demonstrating that NIR light can be rapidly and efficiently converted into

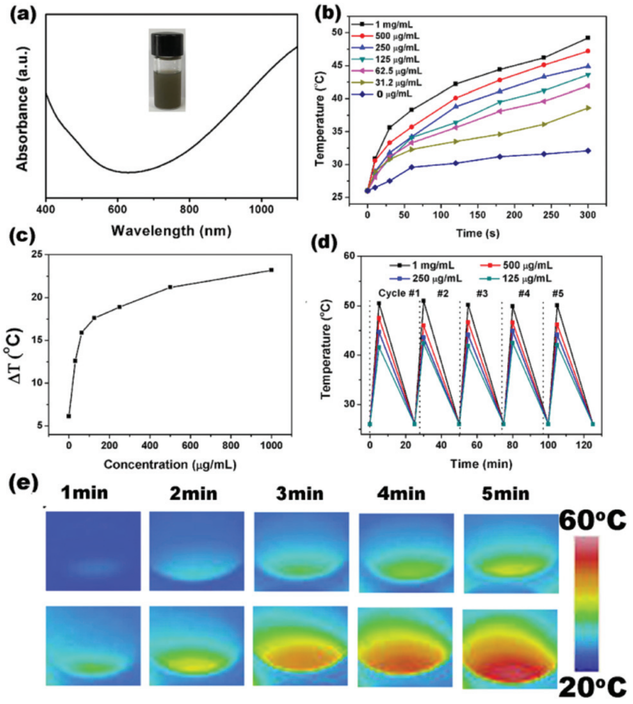

**Fig. 3** (a) The UV-Vis-NIR absorption spectra of the $Cu_9S_5@mSiO_2$ nanocomposite (0.5 mg $mL^{-1}$) and a image of the $Cu_9S_5@mSiO_2$ sample in an aqueous solution under ambient light (inset). (b) Temperature variation curves for the aqueous dispersions containing CMF at different concentrations under irradiation at 980 nm with a power density of 0.76 W $cm^{-2}$ as a function of the irradiation time. (c) A plot of temperature elevation over a period of 300 s *versus* the concentration of the CMF nanocomposite. (d) Temperature changes of CMF at different concentrations over five ON/OFF cycles using 980 nm laser irradiation. (e) Infrared thermal images of PBS (up) and the CMF solution (down) *versus* different NIR irradiation times.

thermal energy by the CMF nanocomposite without causing a significant temperature increase in pure water. It is generally accepted that 980 nm is not a good candidate and is only used in experiments that need a long laser exposure time and/or very high power density. In the present system, a relatively low power density of 0.76 W $cm^{-2}$ was applied. Under such mild conditions, the final temperature of pure water after irradiation can be deemed safe, indicating that 980 nm can be used safely for photothermal therapy. This is very necessary for the purpose of thermal treatment. Moreover, as an effective photothermal agent, it is also important to assess if repeated irradiation can affect the photothermal efficiency.[37] To simulate this scenario, CMF samples at different concentrations were irradiated with an NIR laser light at 0.76 W $cm^{-2}$ for multiple times (up to five cycles). In each heating cycle, the NIR light irradiation was applied for 5 min followed by a 20 min cooling period (within which the solutions reached room temperature again). From Fig. 3d, we can observe that by repeating the laser on–off cycles, the temperature was increased at each step without compromising the photothermal efficiency significantly, indicating that the repeated irradiation is unable to significantly influence the photothermal properties of the CMF nanocomposite. Fig. 3e also shows the *in vitro* infrared thermal images of both PBS and CMF solutions as a function of the exposure time under laser irradiation at 980 nm. It is apparent that the CMF group has an obviously higher temperature than the PBS group under the same irradiation conditions, which was attributed to the efficient thermal effect of $Cu_9S_5$ induced by NIR light. These results successfully indicate that the as-obtained CMF nanocomposite can serve as a good photothermal agent.

When compared with the previous reports on pure $Cu_9S_5$ nanocrystals, our as-synthesized core–shell CMF nanocomposites do not only possess good optical absorption characteristics and photothermal conversion performance, as described above, but also are expected to have drug loading and magnetically targeted pH-sensitive drug releasing abilities. In this case, doxorubicin hydrochloride (DOX; a water-soluble anticancer drug) was mixed with the CMF core–shell nanocomposite to construct a multifunctional drug system. As expected, the DOX can be effectively loaded into the mesoporous $SiO_2$ shell of the CMF nanoparticles. To evaluate the loading capacity of DOX in the as-obtained CMF nanocarrier, the supernatant and washed solutions were collected, and the residual DOX content ($R_{DOX}$) obtained by UV-vis spectroscopy at a wavelength of 480 nm. Accordingly, the DOX drug loading capacity of the CMF nanocarrier was calculated to be 12%. The final as-obtained DOX loaded CMF nanocomposite (labelled as CMF-DOX) were then dispersed in PBS solution (pH = 7.4 or 5.0) at 37 °C and the drug release percentage evaluated at predetermined time intervals. The results are shown in Fig. 4 from which we can observe that the *in vitro* DOX release profiles of CMF-DOX were obviously pH-dependent. There was 24% of DOX released after 24 h in pH = 5.0 PBS solution, whereas nearly no DOX was released when the pH of PBS solution increased to 7.4. This pH-responsive drug release trend of

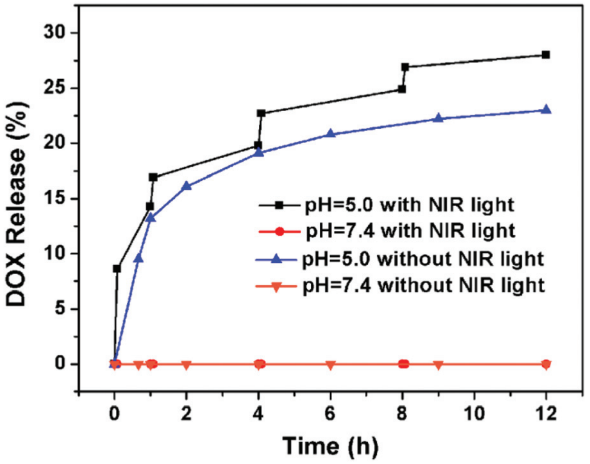

**Fig. 4** Cumulative DOX release from the CMF-DOX nanocomposite in the absence and presence of 980 nm NIR light (5 min, 0.76 W $cm^{-2}$) in pH = 7.4 and pH = 5.0 PBS buffer.

the DOX loaded CMF nanoplatform was mainly attributed to the increased hydrophilicity and higher solubility of DOX in lower pH environment, which was caused by the increased number of protonated $-NH_2$ groups in DOX.[38] For *in vivo* bio-applications, this pH-responsive DOX release profile can ensure that the CMF-DOX nanocomposite remains stable in the physiological environment (pH 7.4), but gradually releases DOX in response to acidic pH once the nanocomposites accumulate in tumor tissues (pH < 6.5) *via* the magnetic tumor targeting and EPR effect. This pH-responsive drug release profile can act as a "barrier" to drug release in a normal physiological environment, decreasing the amount of DOX dissociated from the carrier prior to release in non-target spots during transportation, and reducing the side effects of any chemotherapeutics. In addition, the promotional effect of NIR irradiation on DOX release from CMF-DOX was also observed in Fig. 4. This enhanced drug release upon NIR irradiation can be attributed to the increasing temperature generated by the $Cu_9S_5$ core, which can directly accelerate the speed of desorption or release of DOX molecules from the mesoporous silica shell of CMF for effective anticancer chemotherapy.[39] In this way, the as-synthesized CMF could be used simultaneously as an agent for photothermal therapy and a potential drug carrier for pH/NIR dependent anti-tumor drug release.

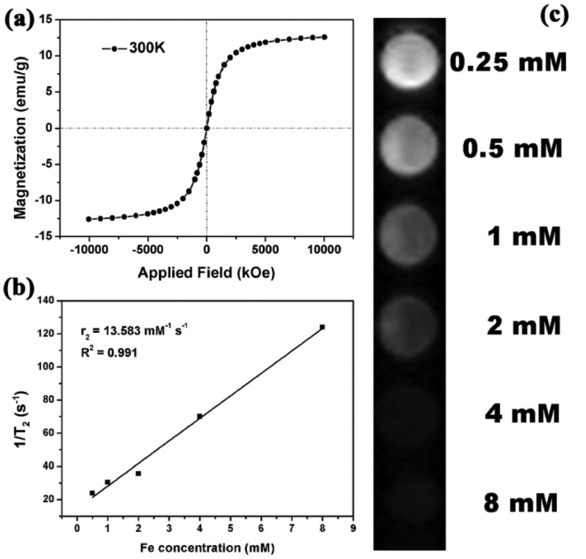

Fig. 5 (a) Magnetization as a function of the applied field for the as-synthesized CMF at 300 K; (b) relaxation rate $R_2$ ($1/T_2$) *versus* the different [Fe] concentrations of CMF at room temperature and (c) the $T_2$-weighted MR images of CMF at different [Fe] concentrations.

### 2.3 *In vitro* MR imaging and combined chemo/photothermal therapy

In recent years, many researchers have focused on imaging assisted NIR nanocarriers for precise cancer diagnosis and location to guide external laser irradiation without damaging the surrounding healthy tissues.[40] Herein, owning to the existence of the $Fe_3O_4$ nanocrystals, the as-obtained CMF nanocomposites possess unique superparamagnetic characteristics, as shown in Fig. 5a, which can be used as an effective $T_2$ contrast agent in MRI by accelerating the transverse relaxation of water protons. Note that a relatively low saturation magnetization was obtained using the CMF nanocomposite, mainly because of the decreased interparticle interactions and the low amount of $Fe_3O_4$ particles on the silica shell. The transverse relaxation time of the protons from the CMF aqueous dispersion at different concentrations was recorded in Fig. 5b and the transverse relaxivity ($r_2$) of CMF calculated to be 13.583 $mM^{-1}$ $S^{-1}$. Furthermore, a concentration-dependent darkening effect of the $T_2$-weighted MR images was observed in Fig. 5c, revealing that the CMF nanoparticles can act as a useful $T_2$ contrast agent for MR imaging. In this way, the obtained CMF nanocomposite can help to integrate both MRI diagnosis and chemo/photothermal therapy into a single multimodal nanoplatform to construct so-called "theranostic" platform, which can help to diagnose and locate the cancer disease and visualize nanoparticle accumulation.

Because the toxicology of CMF is very important in their further bio-applications, an MTT assay of HeLa cells was employed. As shown in Fig. 6a, the cell viability of CMF stained HeLa cells was still high when the concentration of the

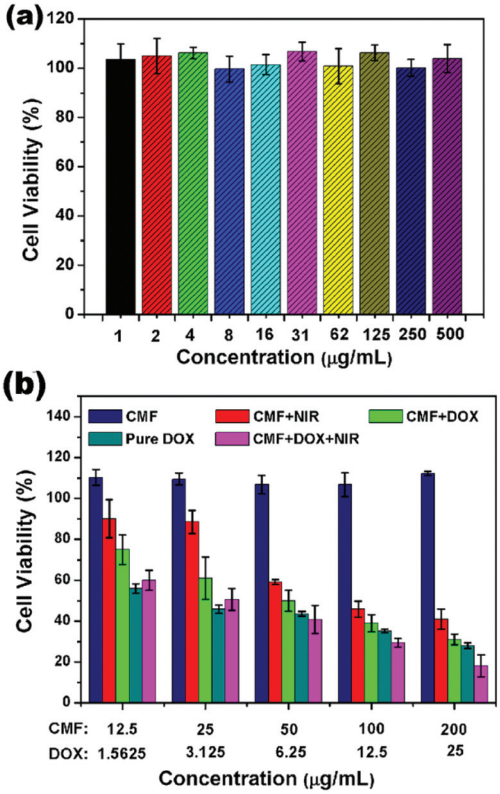

Fig. 6 (a) *In vitro* cell viability data of cultured HeLa cells after incubation with CMF for 24 h using a standard MTT colorimetric assay. (b) *In vitro* cytotoxicity of CMF, CMF + NIR, CMF + DOX, free DOX, and CMF + DOX + NIR against HeLa cells after 24 h of incubation.

CMF was as high as 500 μg $mL^{-1}$ after the 24 h of culture, confirming the non-cytotoxicity of CMF. After that, the cytotoxic effect of CMF-DOX against HeLa cells under the NIR light irradiation was evaluated using the MTT tests as well. After the treatment of pure CMF, CMF + NIR, CMF + DOX, pure DOX or CMF + DOX + NIR for 24 h, the *in vitro* cytotoxic effect of each group was evaluated and the results are shown in Fig. 6b: (i) the group of HeLa cells treated with CMF alone had no significant cell death under all the concentrations studied; (ii) the group of HeLa cells incubated with CMF under NIR irradiation had a moderate cell death with almost 40% of the cells still viable up to a concentration of 200 μg $mL^{-1}$; (iii) the DOX loaded CMF had comparable cytotoxicity with free DOX at the same concentration of DOX, which indicated that the DOX loaded CMF was pharmacologically active as a potential drug carrier; (iv) the group of cells incubated with CMF-DOX and 10 min laser irradiation caused a much higher cell death when compared to any of the above mentioned groups and less than 20% of the cells were still viable up to the concentration of 200 μg $mL^{-1}$. This increased cell ablation ability can contribute to the better therapeutic effects of the combined chemo/photothermal therapy.

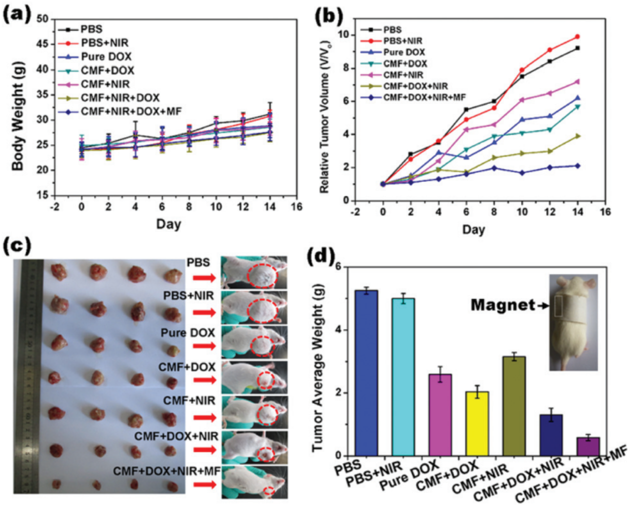

**Fig. 7** The body weights (a) and the relative tumor volumes (b) of mice after treatment with PBS (as the control), PBS + NIR, free DOX, CMF + DOX, CMF + NIR, CMF + DOX + NIR and CMF + DOX + NIR + MF, respectively. (c) Images of the excised tumors and representative Kunming mice with different treatments at the last day of experiments. (d) Mean tumor weights of each group at the last day of experiments. The inset of (d) is an image of a mouse treated with magnetic tumor targeting.

### 2.4 *In vivo* targeted chemo/photothermal therapy efficacy of CMF-DOX

Having shown the outstanding synergistic effect of the chemo/photothermal therapy *in vitro*, we next investigated the tumoricidal efficacy of CMF-DOX *in vivo* using a H22 (murine hepatocarcinoma) xenograft model developed by injecting H22 cancer cells in the left axilla of Kunming mice. In detail, the tumor-bearing mice were divided into seven randomized groups ($n$ = 5, each group), respectively, treated with pure PBS (control group), PBS under 980 nm laser (PBS + NIR), free DOX, DOX loading CMF nanocomposites (CMF-DOX), CMF under 980 nm laser (CMF + NIR), CMF-DOX under 980 nm laser (CMF-DOX + NIR) and CMF-DOX + NIR with a tumor-targeted magnet (CMF-DOX + NIR + MF). Note that for the NIR irradiation groups, we irradiated the tumor site using a 980 nm laser (0.76 W $cm^{-2}$) for 10 min, 1 h after the injection. To assure the antitumor efficiency,[41] the use of $Fe_3O_4$ magnetic nanoparticles was achieved for the magnetically targeted chemo/photothermal therapy by adding a magnet right outside the tumor (inset in Fig. 7d). During the experiments, the body weights and tumor volumes of the mice were monitored every two days and the results recorded in Fig. 7a and b. The variation trends in the mean body weight (Fig. 7a) show that the weights of the mice in all seven groups increased slowly with similar increase trends. However, the tumor volumes of each group varied with their own characteristics (Fig. 7b). The mice treated with PBS solution only or PBS + NIR exhibited rapidly increasing tumor volumes, whereas the following three treated groups: pure DOX, CMF + DOX and CMF + NIR show a slight inhibition of tumor growth, indicating that a single therapeutic approach alone, either photothermal therapy or chemotherapy, can suppress the tumor growth to some degree, but has a relatively poor efficacy. For the group treated with CMF-DOX under NIR light, namely, the CMF + NIR + DOX group, an enhanced inhibition of tumor growth was observed demonstrating that the combined chemo/photothermal therapy has a highly superior inhibition of the animal H22 tumor *in vivo* to any of the single approaches. With the magnetic field turned on, the so-called CMF + NIR + DOX + MF group showed the lowest tumor growth rate over a course of 14 days, implying that the as-obtained CMF-DOX nanocomposites with a tumor-targeted magnetic field outside have a highly superior inhibition of the animal H22 tumor *in vivo*.

The images and average weights of the final tumors excised from mice of each group can further verify the above-mentioned conclusions. As shown in Fig. 7c, it is clearly observed that the CMF + NIR + DOX + MF group has the smallest volume of tumors when compared with the other six groups. An effective tumor growth inhibition rate of 89% in the CMF + NIR + DOX + MF group can also be observed, as shown in Fig. 7d, which was much higher than the CMF + NIR + DOX group with an inhibition efficacy of 75.2% and the other treated groups with even lower inhibition efficacies.

The results come from the following two expectations: on one hand, the synergistic effect of combining photothermal therapy and chemotherapy in our drug delivery system helps to improve the inhibition efficacy of tumor growth; whereas on the other hand, the magnetic fields generated by the magnet attached right outside the tumor can help to attract those nanospheres from the circulating blood to a specific region, which would be of great importance for the further anti-tumor therapy.

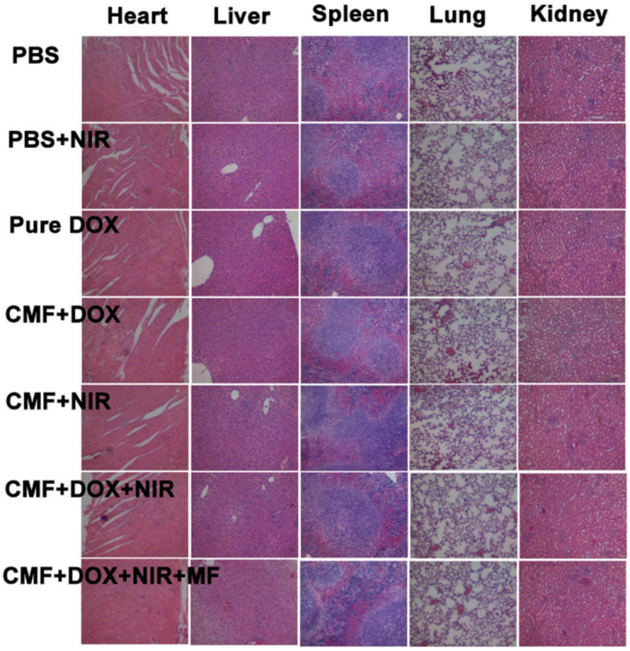

**Fig. 8** Haematoxylin and Eosin (H&E) stained images of the major organs studied for the PBS, PBS + NIR, free DOX, CMF + DOX, CMF + NIR, CMF + DOX + NIR and CMF + DOX + NIR + MF groups.

With the excellent synergistic therapeutic performance of this nanocarrier system, the *in vivo* toxicity should be well investigated before they find their way into clinical applications. Based on this line, Haematoxylin and Eosin (H&E) staining of the main organs, including the heart, liver, spleen, lung, and kidney, in the respective seven groups were carried out. As we can observe from Fig. 8, there was no obvious histological lesion or any other adverse effect in the histological samples analysed, indicating that the as-obtained nanoparticles have excellent *in vivo* biocompatibility and can be used as a highly active drug delivery carrier for anticancer therapy. In conclusion, CMF nanoparticles have emerged as promising candidates as a magnetically targeted synergistic therapeutic agent in biological medicine applications because of their excellent anticancer therapy and eminent safety.

## 3. Conclusions

We have successfully constructed a mono-dispersed magnetically targeted nanocarrier system, $Cu_9S_5$@m$SiO_2$@$Fe_3O_4$-PEG (CMF), which can simultaneously achieve NIR triggered photothermal therapy, pH/NIR-responsive chemotherapy and MR imaging to enhance the therapeutic efficacy. Upon irradiation using 980 nm NIR light, the photothermal effect of $Cu_9S_5$ did not only generate a rapid rise in the local temperature to “cook” cancer cells, but also result in an accelerated release of cytotoxic DOX, exhibiting a synergistic therapy for Hela cells *in vitro*. Under the influence of an external magnetic field, the as-obtained synergistic therapeutic effect of CMF-DOX can be used to successfully control the growth of subcutaneous tumors in 14 days following a single 10 min NIR irradiation. This magnetically targeted capability for combined chemo/photothermal therapy may help to pave the way towards more effective nanotherapeutics. Histological analysis also revealed no pathological changes and inflammatory response in heart, lung, kidney, liver and spleen tissues. Such a nanoplatform with convenient synthesis, good biocompatibility, low cytotoxic activity and low cost, effective MR imaging, together with the improved *in vitro*/*in vivo* magnetically targeted chemo/photothermal synergistic therapy efficiency, is expected to open a new way for effective cancer treatment.

## 4. Experimental

### 4.1 Materials

All the chemical reagents were used as received without further purification. Oleylamine (OM), oleic acid (OA), octadecene (ODE), 3-aminopropyltriethoxysilane (APTES), ferric acetylacetonate (Fe(acac)$_3$) and 2-bromo-2-methyl-propionic acid (BMPA) were purchased from Sigma-Aldrich. Doxorubicin hydrochloride (DOX) was purchased from Nanjing Duodian Chemical Limited Company (China). Sulfur (S), copper(I)-chloride (CuCl), cetyltrimethylammonium bromide (CTAB), tetraethylorthosilicate (TEOS), sodium hydroxide (NaOH), ammonium hydroxide ($NH_3 \cdot H_2O$), citrate acid ($C_6H_8O_7$), cyclohexane, ammonium nitrate ($NH_4NO_3$), sodium chloride (NaCl), potassium chloride (KCl) and other reagents used in the study were all purchased from Beijing Fine Chemical Regent Company (China).

### 4.2 Preparation of the $Cu_9S_5$@m$SiO_2$-$NH_2$ nanoparticles

Uniform $Cu_9S_5$ nanoparticles with sizes of about 18 nm were fabricated according to the reported previously method with slight modification.[42] The modified synthetic method is described as follows: first, CuCl (1 g), 4 mL of OM and 5 mL of OA were mixed under magnetic stirring and heated up to 130 °C under air free conditions. Once the temperature reached at 130 °C, the as-prepared copper precursor was cooled down to room temperature and reserved for further use. Second, sulfur powder (0.32 g) and ODE (40 mL) were mixed at 200 °C under a $N_2$ atmosphere, following a typical swift hot-injection of the as-prepared copper precursor. The as-obtained mixture was kept at 200 °C for 30 min, resulting in a black colloidal solution. Then, the as-obtained colloidal solution was cooled down to room temperature and precipitated using excess ethanol. The precipitate was re-dispersed in 20 mL of chloroform.

$Cu_9S_5$@m$SiO_2$ nanocomposite spheres were successfully synthesized using a modified method described previously.[43,44] The as-prepared $Cu_9S_5$@m$SiO_2$ nanocomposites were finally dispersed in 20 mL of ethanol. To functionalize the $Cu_9S_5$@m$SiO_2$ nanospheres with amine groups for the further reaction, 200 μL of APTES was added into 20 mL of an ethanol solution containing the $Cu_9S_5$@m$SiO_2$ nanospheres with stirring overnight. The resulting $Cu_9S_5@mSiO_2\text{-}NH_2$ nanocrystals were obtained by centrifugation and re-dispersed in 10 mL of ethanol for the further use.

### 4.3 Preparation of the $Cu_9S_5@mSiO_2@Fe_3O_4$-PEG (CMF) nanoparticles

The CMF nanocomposite was successfully prepared as follows: (i) a mixed solution containing OA (1.5 mL), OM (1.5 mL), benzyl alcohol (10 mL) and $Fe(acac)_3$ (0.353 g) was sealed in a Teflon bottle and maintained at 180 °C for 10 h. (ii) The as-obtained $Fe_3O_4$-OA nanocrystals were then mixed with 0.5 g of BMPA, 0.05 g of citrate acid in chloroform and a DMF/chloroform mixed solution (16 mL, chloroform : DMF = 1 : 1), and kept stirring for 12 h to obtain BMPA-capped $Fe_3O_4$ nanocrystals.[45] (iii) The as-obtained BMPA modified $Fe_3O_4$ nanocrystals were added to the $Cu_9S_5@mSiO_2\text{-}NH_2$ ethanol solution and stirred overnight. The obtained $Cu_9S_5@mSiO_2@Fe_3O_4$ nanoparticles were redispersed in 20 mL of ethanol. (iv) PEG-SC (20 mg) was finally stabilized on the surface of the $Cu_9S_5@mSiO_2@Fe_3O_4$ nanoparticles to obtain the CMF nanoparticles. The resulting CMF were dispersed in 10 mL of water.

### 4.4 Photothermal heating experiments of the CMF nanoparticles

CMF aqueous solutions at different concentrations were suspended in different wells of a 96-well plate, irradiated using a 980 nm laser with an irradiation density of 0.76 W $cm^{-2}$ for different durations. The concentration of the CMF solutions were 15.6, 31.2, 62.5, 125, 250, 500 and 1000 μg $mL^{-1}$, and the irradiation times were 10 s, 30 s, 1 min, 2 min, 3 min, 4 min and 5 min, respectively. The temperatures of all the different CMF concentrations under different irradiation times were carefully measured using a digital thermometer with a thermocouple probe. To assess if repeated irradiation can affect the photothermal efficiency of CMF, the CMF samples at different concentrations were irradiated with NIR laser light at 0.76 W $cm^{-2}$ multiple times (up to five cycles). In each heating cycle, 980 nm light irradiation was applied for 5 min followed by a 20 min cooling period (within which the solutions reached room temperature again). The temperatures were also carefully measured using a digital thermometer with a thermocouple probe.

### 4.5 Anticancer drug storage and pH/NIR-triggered drug release

The protocol to prepare PBS at different pH values is illustrated as follows: 8 g of NaCl, 0.2 g of KCl, 2.9 g of $Na_2HPO_4$ and 0.2 g of $KH_2PO_4$ were mixed into 1 L of deionized water and stirred for 1 h. After mixing evenly, a moderate amount of HCl diluent was added to adjust the pH value. For DOX drug storage, the as-obtained CMF (10 mg) was mixed with 2 mL of free DOX aqueous solution (1 mg $mL^{-1}$) under magnetic stirring at 37 °C for 12 h. The excess amount of DOX was removed by centrifugation and the supernatant was collected to determine the loaded amount of free DOX using UV-Vis spectroscopy. The DOX-loading capacity of CMF was calculated as follows: $[(O_{DOX} - R_{DOX})/(M_{CMF} + O_{DOX} - R_{DOX})] \times 100\%$, in which $M_{CMF}$ is the CMF content, $O_{DOX}$ is the original DOX content, $R_{DOX}$ is the residual DOX content. The obtained DOX loaded CMF were collected and denoted as CMF-DOX. The pH-responsive drug release experiments were carried out by dispersing the CMF-DOX in 2 mL of pH = 7.4 or pH = 5.0 PBS with gentle shaking. After centrifugation of the CMF-DOX PBS solution for a pre-planned time, the original PBS was replaced by 2 mL of fresh PBS and the absorbance of the original PBS measured using UV-Vis spectroscopy at a wavelength of 480 nm. Similarly, the NIR-light-triggered drug release from the CMF-DOX nanoparticles was carried out as follows: the 980 nm laser probe was fixed 3 cm from the center of the tube, which was filled with the PBS solution containing CMF-DOX. The samples were irradiated with the 980 nm NIR laser for 5 min and subsequently centrifuged at 7000 rpm for 4 min. The released free DOX was quantified using UV-Vis spectroscopy at a wavelength of 480 nm.

### 4.6 *In vitro* magnetic resonance (MR) imaging

CMF aqueous solutions with various Fe concentrations were prepared in 1.5 mL centrifuge tubes for the tests. The molar concentrations of Fe in the CMF solutions were determined by ICP-AES. $T_2$-Weighted MR imaging experiments of the CMF were achieved using a 0.5 T MRI magnet (Shanghai Niumai Corporation Ration NM120-Analyst). Both the $T_2$-weighted MR images and relaxation time $T_2$ values were obtained.

### 4.7 *In vitro* cytotoxicity of the CMF

The biocompatibility of the synthesized CMF was determined using a standard MTT test.[46] HeLa cells were incubated in fresh DMEM culture medium containing CMF (at different concentrations of 7.8, 15.6, 31.2, 62.5, 125, 250, and 500 μg $mL^{-1}$) for 24 h. The viability of the HeLa cells was evaluated using a microplate reader. The cytotoxicity of CMF-DOX was also detected using the MTT cell assay as described above. HeLa cells were seeded in a 96-well plate (8000 cells per well) and treated with fresh DMEM culture medium containing the desired amount of free DOX, CMF-DOX and pure CMF. For the photothermal heating experiments, after incubation for 4 h, the excess unbound CMF or CMF + DOX nanoparticles were removed by rinsing three times with PBS. Fresh culture medium was then added into the wells. The cells were exposed to NIR light (0.76 W $cm^{-2}$) for 10 min to achieve photothermal or chemo-photothermal treatments and then incubated again at 37 °C with 5% $CO_2$ for 24 h. Finally, the viability of the HeLa cells was evaluated using a microplate reader at 490 nm.

### 4.8 *In vivo* antitumor efficacy of CMF-DOX

Kunming mice with an average weight of 20 g were purchased from Jilin University (Changchun, China). Animal procedures were in agreement with the guidelines of The National Regulation of China for Care and Use of Laboratory Animals. H22 cells (murine hepatocarcinoma cell lines) suspended in PBS (150 μL) were inoculated subcutaneously in the left axilla of female Kunming mice. The tumors were allowed to grow for 5 days to reach a size of around 100 $mm^3$. Then, the tumor-bearing mice were divided into seven randomized groups ($n$ = 5, each group), which were PBS treated (control group), PBS treated with 980 nm laser (PBS + NIR), free DOX treated, CMF-DOX treated, CMF treated with 980 nm laser (CMF + NIR), CMF-DOX treated with 980 nm laser (CMF-DOX + NIR) and CMF-DOX treated with 980 nm laser with a tumor-targeted magnet (CMF-DOX + NIR + MF). For the tail vein injection model, the mice were injected with PBS, CMF and CMF + DOX aqueous dispersion two times on day 1 and day 4. Each time the DOX dose was controlled at 4.0 mg per kg body weight. For the NIR irradiation, we irradiated the tumor site with the 980 nm laser (0.76 W cm$^{-2}$) for 10 min, 1 h after injection of the different materials. The tumor dimensions were tracked with a caliper for 14 d. The tumor volume was calculated according to the formula: tumor volume ($V$) = (tumor length) × (tumor width)$^2$/2. The relative tumor volumes were calculated as $V/V_0$ ($V_0$ was the tumor volume when the treatment was initiated). Furthermore, histological examination was also carried out to evaluate the safety of CMF. Major organs of mice (heart, liver, spleen, lung and kidney) in each group were collected and fixed in 4% paraformaldehyde solution after 14 d of treatment for the further tests.

### 4.9 Characterization

The X-ray diffraction (XRD) patterns of the samples were obtained using a D8 Focus diffractometer (Bruker) with Cu Kα radiation ($\lambda$ = 0.15405 nm). The UV-vis adsorption spectra values were carried out on a U-3310 spectrophotometer. Transmission electron microscopy (TEM) was obtained using a FEI Tecnai G2 S-Twin transmission electron microscope with a field emission gun operating at 200 kV. Nitrogen adsorption/desorption analysis was carried out using a Micromeritics ASAP 2020 M apparatus. MTT experiments were carried out using a microplate reader (Thermo Multiskan MK3). All the measurements were carried out at room temperature.

## Acknowledgements

This study is financially supported by the National Natural Science Foundation of China (NSFC 51332008, 51472231, 51372243, 51422209, 51572258) and the National Basic Research Program of China (2014CB643803).

## Notes and references

1 J. Liu, W. Bu, L. Pan and J. Shi, *Angew. Chem., Int. Ed.*, 2013, **52**, 4375.

2 Y. Wang, S. Song, J. Liu, D. Liu and H. Zhang, *Angew. Chem., Int. Ed.*, 2015, **54**, 536.

3 L. Du, S. Liao, H. A. Khatib, J. F. Stoddart and J. I. Zink, *J. Am. Chem. Soc.*, 2009, **131**, 15136.

4 J. Liu, X. Zheng, L. Yan, L. Zhou, G. Tian, W. Yin, L. Wang, Y. Liu, Z. Hu, Z. Gu, C. Chen and Y. Zhao, *ACS Nano*, 2015, **9**, 696.

5 L. Cheng, J. Liu, X. Gu, H. Gong, X. Shi, T. Liu, C. Wang, X. Wang, G. Liu, H. Xing, W. Bu, B. Sun and Z. Liu, *Adv. Mater.*, 2014, **26**, 1886.

6 L. S. Lin, Z. X. Cong, J. B. Cao, K. M. Ke, Q. L. Peng, J. Gao, H. H. Yang, G. Liu and X. Chen, *ACS Nano*, 2014, **8**, 3876.

7 J. Liu, C. Detrembleur, M. C. De Pauw-Gillet, S. Mornet, C. Jérôme and E. Duguet, *Small*, 2015, **11**, 2323.

8 Z. Jiang, B. Dong, B. Chen, J. Wang, L. Xu, S. Zhang and H. Song, *Small*, 2013, **9**, 604.

9 M. Li, H. Yan, C. Teh, V. Korzh and Y. Zhao, *Chem. Commun.*, 2014, **50**, 9745.

10 J. Liu, C. Wang, X. Wang, X. Wang, L. Cheng, Y. Li and Z. Liu, *Adv. Funct. Mater.*, 2014, **25**, 384.

11 X. Zhang, L. Song, L. Cai, X. Tian, Q. Zhang, X. Qi, W. Zhou, N. Zhang, F. Yang, Q. Fan, Y. Wang, H. Liu, X. Bai, W. Zhou and S. Xie, *Light: Sci. Appl.*, 2015, **4**, e318.

12 L. Li, Y. Liu, P. Hao, Z. Wang, L. Fu, Z. Ma and J. Zhou, *Biomaterials*, 2015, **41**, 132.

13 K. Yang, H. Xu, L. Cheng, C. Sun, J. Wang and Z. Liu, *Adv. Mater.*, 2012, **24**, 5586.

14 H. Li, R. Brescia, M. Povia, M. Prato, G. Bertoni, L. Manna and I. Moreels, *J. Am. Chem. Soc.*, 2013, **135**, 12270.

15 X. Liu, Q. Wang, C. Li, R. Zou, B. Li, G. Song, K. Xu, Y. Zheng and J. Hu, *Nanoscale*, 2014, **6**, 4361.

16 X. Liu, F. Fu, K. Xu, R. Zou, J. Yang, Q. Wang, Q. Liu, Z. Xiao and J. Hu, *J. Mater. Chem. B*, 2014, **2**, 5358.

17 Q. Xiao, X. Zheng, W. Bu, W. Ge, S. Zhang, F. Chen, H. Xing, Q. Ren, W. Fan, K. Zhao, Y. Hua and J. Shi, *J. Am. Chem. Soc.*, 2013, **135**, 13041.

18 L. Wu, M. Wu, Y. Zeng, D. Zhang, A. Zheng, X. Liu and J. Liu, *Nanotechnology*, 2015, **26**, 025102.

19 J. Mou, P. Li, C. Liu, H. Xu, L. Song, J. Wang, K. Zhang, Y. Chen, J. Shi and H. Chen, *Small*, 2015, **11**, 2275.

20 R. Chen, X. Zheng, H. Qian, X. Wang, J. Wang and X. Jiang, *Biomaterials*, 2013, **1**, 285.

21 Y. Wang, K. Wang, J. Zhao, X. Liu, J. Bu, X. Yan and R. Huang, *J. Am. Chem. Soc.*, 2013, **135**, 4799.

22 H. Liu, D. Chen, L. Li, T. Liu, L. Tan, X. Wu and F. Tang, *Angew. Chem., Int. Ed.*, 2011, **50**, 891.

23 K. Dong, Z. Liu, Z. Li, J. Ren and X. Qu, *Adv. Mater.*, 2013, **25**, 4452.

24 X. Liu, Q. Wang, C. Li, R. Zou, B. Li, G. Song, K. Xu, Y. Zheng and J. Hu, *Nanoscale*, 2014, **6**, 4361.

25 H. Y. Liu, D. Chen, L. L. Li, T. L. Liu, L. F. Tan, X. L. Wu and F. Q. Tang, *Angew. Chem., Int. Ed.*, 2011, **50**, 891.

26 H. Y. Liu, T. L. Liu, X. L. Wu, L. L. Li, L. F. Tan, D. Chen and F. Q. Tang, *Adv. Mater.*, 2012, **24**, 755.

27 M. Ma, H. Chen, Y. Chen, X. Wang, F. Chen, X. Cui and J. Shi, *Biomaterials*, 2012, **33**, 989.

28 Y. Deng, Y. Cai, Z. Sun and D. Zhao, *Chem. Phys. Lett.*, 2011, **510**, 1.

29 H. Liu, T. Liu, X. Wu, L. Li, L. Tan, D. Chen and F. Tang, *Adv. Mater.*, 2012, **24**, 755.

30 Y. Chen, H. Chen, S. Zhang, F. Chen, L. Zhang, J. Zhang, M. Zhu, H. Wu, L. Guo, J. Feng and J. Shi, *Adv. Funct. Mater.*, 2011, **21**, 270.

31 C. C. Huang, C. Y. Tsai, H. S. Sheu, K. Y. Chuang, C. H. Su, U. S. Jeng, F. Y. Cheng, C. H. Su, H. Y. Lei and C. S. Yeh, *ACS Nano*, 2011, **5**, 3905.

32 X. Zhu, J. Zhou, M. Chen, M. Shi, W. Feng and F. Li, *Biomaterials*, 2012, **33**, 4618.

33 Y. Wang and H. Gu, *Adv. Mater.*, 2015, **27**, 573.

34 C. X. Li, D. M. Yang, P. A. Ma, Y. Y. Chen, Y. Wu, Z. Y. Hou, Y. L. Dai, J. H. Zhao, C. P. Sui and J. Lin, *Small*, 2013, **9**, 4150.

35 G. Song, Q. Wang, Y. Wang, G. Lv, C. Li, R. Zou, Z. Chen, Z. Qin, K. Huo, R. Hu and J. Hu, *Adv. Funct. Mater.*, 2013, **23**, 4281.

36 D. Jaque, L. Martinez Maestro, B. del Rosal, P. Haro-Gonzalez, A. Benayas, J. L. Plaza, E. Martin Rodriguez and J. Garcia Sole, *Nanoscale*, 2014, **6**, 9494.

37 X. Liu, B. Li, F. Fu, K. Xu, R. Zou, Q. Wang, B. Zhang, Z. Chen and J. Hu, *Dalton Trans.*, 2014, **43**, 11709.

38 B. Liu, C. Li, D. Yang, Z. Hou, P. a. Ma, Z. Cheng, H. Lian, S. Huang and J. Lin, *Eur. J. Inorg. Chem.*, 2014, **2014**, 1906.

39 L. Wu, M. Wu, Y. Zeng, D. Zhang, A. Zheng, X. Liu and J. Liu, *Nanotechnology*, 2015, **26**, 025102.

40 C. Caltagirone, A. Bettoschi, A. Garau and R. Montis, *Chem. Soc. Rev.*, 2015, **44**, 4645.

41 T. Gulin-Sarfraz, J. Zhang, D. Desai, J. Teuho, J. Sarfraz, H. Jiang, C. Zhang, C. Sahlgren, M. Linden, H. Gu and J. M. Rosenholm, *Biomaterials*, 2014, **2**, 1750.

42 L. Liu, H. Zhong, Z. Bai, T. Zhang, W. Fu, L. Shi, H. Xie, L. Deng and B. Zou, *Chem. Mater.*, 2013, **25**, 4828.

43 B. Liu, C. Li, p. Ma, Y. Chen, Y. Zhang, Z. Hou, S. Huang and J. Lin, *Nanoscale*, 2015, **7**, 1839.

44 Y. Chen, Z. Hou, B. Liu, S. Huang, C. Li and J. Lin, *Dalton Trans.*, 2015, **44**, 3118.

45 J. E. Lee, N. Lee, H. Kim, J. Kim, S. H. Choi, J. H. Kim, T. Kim, I. C. Song, S. P. Park, W. K. Moon and T. Hyeon, *J. Am. Chem. Soc.*, 2009, **132**, 552.

46 K. Yang, H. Xu, L. Cheng, C. Sun, J. Wang and Z. Liu, *Adv. Mater.*, 2012, **24**, 5586.